

Charge Oscillation Induced Superconductivity in Multi-layer Graphene

Ziyan Li,^{1,2} Xueheng Kuang,^{1,2} Zhen Zhan,¹ Shengjun Yuan,^{1,3} and Francisco Guinea^{2,4,5}

¹Key Laboratory of Artificial Micro- and Nano-structures of the Ministry of Education and School of Physics and Technology, Wuhan University, Wuhan 430072, China

²Imdea Nanoscience, C/ Faraday 9, 28015 Madrid, Spain

³Wuhan Institute of Quantum Technology, Wuhan 430206, China

⁴Donostia International Physics Center, Paseo Manuel de Lardizábal 4, 20018 San Sebastián, Spain

⁵Ikerbasque. Basque Foundation for Science. 48009 Bilbao. Spain.

(Dated: December 14, 2022)

Motivated by the recent experimental detection of superconductivity in AB-stacked and ABC-stacked graphene, we study the critical temperatures (T_c) and order parameters (OP) in multi-layer graphene based on the Kohn-Luttinger-Like mechanism. We assume that the acoustic phonon induced charge oscillation contributes the most to the screened electron-electron interaction between Cooper pairings, leading to the emergence of superconductivity in these non-twisted graphene systems. The metallic gates screening and electron-hole excitation are also considered to fully investigate the screening effect. We compare the calculated T_c in graphene with different stacking methods and find that rhombohedral-stacked (ABC and ABCA) graphene perform higher critical temperatures in the order of 10^2 mK. The higher density of state (DOS) peaks appearing in these rhombohedral-stacked graphene systems strongly account for their higher T_c . We further explore the order parameters which change sign within each valley and display inter-valley A_2 symmetry, indicating the f-wave or p-wave superconductivity in multi-layer graphene systems.

I. INTRODUCTION

The superconductivity in non-twisted AB-stacked and ABC-stacked graphenes have been studied experimentally [1–3] recently, with $T_c = 26$ mK and $T_c = 106$ mK respectively. Compared with twisted multi-layer graphene whose signatures of superconductivity are sensitive to local layer migration and the angle twisted [4], the observation of non-twisted graphene superconductivity is much easier to conduct, which encourages us to focus again on the superconductivity computation in these non-twisted systems with more experimental results to support our theoretical mechanism. Several theoretical work [5–8] with various mechanisms has been done to investigate the mechanism accounting for the appearing superconductivity in these non-twisted graphene. As discussed in these references, acoustic-phonon mechanism [5, 9], repulsive Coulomb interactions [10], directly screened potential [11] and spin-orbit enhancement [6] will help account for the attractive electron pairing interaction in graphene systems. All the mechanisms make the proposal about the van Hove singularity (VHS) induced by an applied bias, corresponding to the emergence of the partial flat band close to CNP. The band dispersion near the VHS will lead to a large DOS peak favoring more correlated electronic phases, which account for the enhanced attractive pairing interaction and superconductivity [12] in the graphene system.

Motivated by the phonon induced charge oscillation discussed in the Ref. [8], we assume the charge oscillation mediated by the acoustic phonon-electron coupling [8, 13] contributes the most to the superconductivity. The influence of metallic gates screening [14] and electron-hole excitation [15] are also considered through Feynman diagrams to fully analyze the screened electron-electron interaction. To support this assumption, we apply the Kohn-Luttinger-Like mechanism [16] to investigate the superconductivity in AB-stacked graphene. We obtain maximum $T_c = 21.6$ mK. Compared

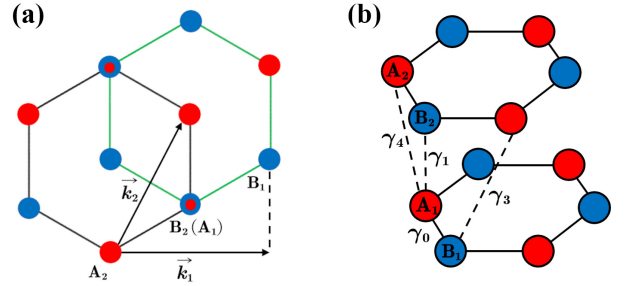


FIG. 1. The lattice structure of AB bilayer graphene. (a) The 2D crystal structure of AB bilayer graphene, with \vec{k}_1 and \vec{k}_2 representing the primitive translation vectors. (b) The 3D crystal structure and some representative hopping parameters between atoms.

with former work focusing on the superconductivity already detected experimentally, we further predict the critical temperatures in ABA-stacked graphene and tetra-layer graphene without existed experimental detection. We find that rhombohedral (ABC and ABCA) stacked graphenes have higher T_c in the order of 10^2 mK than other tri-layer or tetra-layer graphene, which also provide guidance on the future experimental superconductivity detections. Another highlight of our work is the numerical solution of the BCS linearized gap equation instead of analytical formulas with approximation techniques [5], resulting in our calculation results closer to the experimental detection. The order parameter in AB-stacked graphene is further studied to behave as p wave symmetry.

TABLE I. The hopping parameters and on-site energy in multi-layer graphene systems [17, 18].

Parameters (eV)	γ_0	γ_1	γ_2	γ_3	γ_4	γ_5	δ
AB Bilayer	3.16	0.381	—	0.380	0.140	—	0.022
ABC/ABA Trilayer	3.10	0.370	-0.032	0.300	0.040	0.050	0.040
ABCA/ABAB Surface bilayer	3.18	0.390	-0.012	0.300	0.040	0.020	0.050
ABCA/ABAB Bulk bilayer	3.18	0.385	-0.012	0.250	0.030	0.020	0.050

II. THE NUMERICAL METHODS

A. Tight-Binding Model

We employ a tight-binding (TB) model to calculate the band structure of multi-layer graphene systems. We briefly introduce this model via the AB-stacked graphene case. The term AB-stacked refers to shifting one of the graphene layers in the direction [19] along one-third of the translation vector $\vec{k}_1 + \vec{k}_2$, as shown in FIG. 1(a). The lattice structure and representative hopping parameters are shown in FIG. 1(b). Each unit cell of AB bilayer graphene consists of four atoms, A_i and B_i ($i = 1, 2$). Taking into account one p_z orbital per atomic site, then the TB Hamiltonian of the AB bilayer graphene is given as a function of the momentum \vec{k} in first BZ [18]:

$$H_{AB}(\vec{k}) = \begin{pmatrix} -\frac{\Delta_1}{2} + \delta & -\gamma_0 u(\vec{k}) & \gamma_4 u(\vec{k}) & \gamma_1 \\ -\gamma_0 u^*(\vec{k}) & -\frac{\Delta_1}{2} & -\gamma_3 u^*(\vec{k}) & \gamma_4 u(\vec{k}) \\ \gamma_4 u^*(\vec{k}) & -\gamma_3 u(\vec{k}) & \frac{\Delta_1}{2} & -\gamma_0 u(\vec{k}) \\ \gamma_1 & \gamma_4 u^*(\vec{k}) & -\gamma_0 u^*(\vec{k}) & \frac{\Delta_1}{2} + \delta \end{pmatrix} \quad (1)$$

where γ_0 describes the nearest neighbor hopping amplitude between the nearest atoms within the same layer, γ_i ($i=1, 3, 4$) refers to the interlayer hopping parameter between atoms from two layers next to each other, and Δ_1 represents the interlayer potential difference between two nearest layers. Such interlayer potential difference Δ_1 could be generated by applying a vertical electric field to the graphene system. δ is the on-site potential that only exists at sites A_1 and B_2 , which has no nearest neighbors on the adjacent layers. The function $u(\vec{k}) = e^{-ik_y a/\sqrt{3}} + 2e^{ik_y a/(2\sqrt{3})} \cos(k_x a/2)$ describes the nearest hopping between carbon atoms with $a = 0.246$ nm and $d_0 = 0.333$ nm are the lattice constant and interlayer distance of graphene, respectively. These parameters are tabulated in Table I. Note that the additional parameters γ_2 and γ_5 that absent in bilayer, are present in trilayer and tetralayer graphene, which indicate the next-nearest interlayer interactions between atoms from the first and third layers. More details about the TB parameters δ and γ_i refer to [17, 18, 20, 21].

B. Screened Coulomb interaction

In this part, we analyze the screening effect on Coulomb interaction by considering metallic gate screening effect [22], electron-hole excitations [23], and acoustic phonons [8, 16].

Metallic gate screening effect

We assume that the Coulomb interaction is induced by two metallic gates at the same distance d from the top and bottom layers [22, 24]. Then, the Fourier transformation of the bare electron-electron Coulomb potential is given by a function of the momentum \vec{q} :

$$V_C(\vec{q}) = \begin{cases} \frac{2\pi e^2}{\epsilon |\vec{q}|} \tanh(|\vec{q}|d), & |\vec{q}| \neq 0 \\ \frac{2\pi e^2}{\epsilon} \frac{d}{1+e^{-|\vec{q}|d}}, & |\vec{q}| = 0 \end{cases} \quad (2)$$

where e is the electron charge, ϵ represents the dielectric constant of the background. We set $d = 40$ nm, which is the value used in experiments [22].

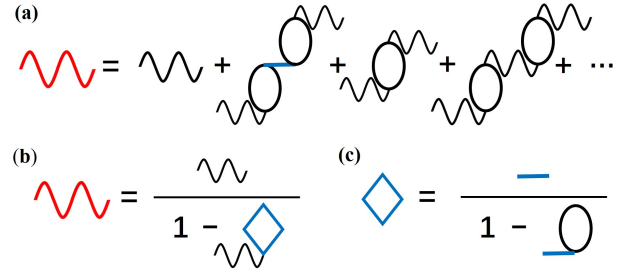


FIG. 2. Feynman diagrams describing the screened Coulomb potential. (a) The red wavy line represents the screened potential while the black wavy line is the metallic gates screened Coulomb potential. (b) Renormalization of the bare Coulomb potential, and the blue diamond describes the screened polarizability. (c) Renormalization of the bare electronic polarizability. The straight blue lines stand for the acoustic phonon-electron coupling.

Electron-phonon interaction effect

In Fig. 2(a), the straight blue lines stand for the long-range acoustic phonons coupling to the electrons, which contributes to the screened Coulomb interaction [8, 16]. In this paper, we only discuss the coupling between longitudinal phonons and electrons due to the deformation potential V_D in the graphene system. This interaction could be described by momentum and frequency-dependent potential $V^{ph}(\vec{q}, \omega)$ given by:

$$V^{ph}(\vec{q}, \omega) = \frac{V_D^2 |\vec{q}|^2}{\rho(\omega^2 - v_s^2 |\vec{q}|^2)} \quad (3)$$

where ρ is the mass density, $v_s = \sqrt{(\lambda_L + 2\mu_L)/\rho}$ is the velocity of sound, λ_L and μ_L are the elastic Lamé coefficients [25]. We set $V_D = 20$ eV and $\lambda_L + 2\mu_L = 2 \times 10^3$ eV · nm⁻²

[8]. Note that we only consider the zero-frequency limit of the Eq. (3), and long-range oscillation with small momentum $|\vec{q}|$:

$$V^{\text{ph}}(\vec{q}) = \begin{cases} -\frac{V_D^2}{\lambda_L + 2\mu_L}, & |\vec{q}| < |\vec{q}_c| \\ 0, & \text{else} \end{cases} \quad (4)$$

Given certain deformation potential and elastic coefficients, $V^{\text{ph}} = -0.2 \text{ eV} \cdot \text{nm}^2$ for momentum $|\vec{q}|$ smaller than $|\vec{q}|_c = |\vec{k}|/10$, where $|\vec{k}|$ is the length of the reciprocal vector. This negative interaction contributes to the minimum screened potential near the center of first BZ, as shown in FIG. 3(c).

Renormalization of Coulomb potential

We apply the static random phase approximation (RPA) method [26–28] to renormalize the Coulomb potential as shown in Fig. 2(b). The screened electron-electron interaction due to electron-hole excitation and acoustic phonon coupling with electrons can be written as:

$$V_{\text{scr}}^{\text{ph}}(\vec{q}) = \frac{V_C(\vec{q})}{1 - V_C(\vec{q})\Pi^{\text{ph}}(\vec{q})} \quad (5)$$

where the polarizability $\Pi^{\text{ph}}(\vec{q})$ including acoustic phonon-electron coupling could be written as the renormalization of the bare electronic polarizability $\Pi^0(\vec{q})$:

$$\Pi^{\text{ph}}(\vec{q}) = \frac{\Pi^0(\vec{q})}{1 - V^{\text{ph}}(\vec{q})\Pi^0(\vec{q})} \quad (6)$$

where the bare electronic polarizability $\Pi^0(\vec{q})$ (the black oval in the Fig. 2(c)) is described as [29–31]:

$$\Pi^0(\vec{q}) = \frac{g_s}{N_C A_C} \sum_{\vec{k}, \text{nm}} \frac{f(\xi_{n,\vec{k}}) - f(\xi_{m,\vec{k}+\vec{q}})}{\epsilon_{n,\vec{k}} - \epsilon_{m,\vec{k}+\vec{q}}} \times \left| \langle \psi_{m,\vec{k}+\vec{q}} | \psi_{n,\vec{k}} \rangle \right|^2 \quad (7)$$

Here $g_s = 2$ stands for the spin degeneracy, N_C is the number of unit cells in the system, $A_C = \frac{\sqrt{3}a^2}{2}$ is the area of each unit cell, $f(\xi_{n,\vec{k}}) = 1/(1 + e^{\xi_{n,\vec{k}}/k_B T})$ is the Fermi-Dirac distribution, with $\xi_{n,\vec{k}} = \epsilon_{n,\vec{k}} - \mu$, μ is the Fermi energy.

As an example, Fig. 3 shows the influence of phonon-electron coupling on the screened electron-electron interaction in AB bi-layer graphene. We use the background dielectric constant $\epsilon = 2.2$ [20] and the inter-layer potential $\Delta_1 = 100 \text{ meV}$. To ensure the convergence of the computation we pick $N_C = 3 \times 10^6$ and the Fermi energy $\mu = 50 \text{ meV}$, which corresponds to the red DOS peak in FIG. 4(b). The screened potential is calculated along the high symmetry path in the first BZ shown in FIG. 3(a). By comparing the Coulomb potentials without and with the phonon effect in FIG. 3, we see that the phonon-electron interaction will induce a more attractive potential. In particular, $V_{\text{scr}}^{\text{ph}}(\vec{q})$ will approach a negative value of $-0.2 \text{ eV} \cdot \text{nm}^2$ when $|\vec{q}| \rightarrow 0$, which implies that the real-space Coulomb potential will be also negative within a range of the horizontal axis. All of these calculated results prove that phonons coupling with electrons will contribute to the attractive electron-electron interaction. To further support

this idea, we further analyze the real-space screened Coulomb potential $V_{\text{scr}}(\vec{r})$ referring to Ref. [6]:

$$V_{\text{scr}}(\vec{r}) = \frac{|\vec{k}|^2}{N_k} \sum_{\vec{k}} V_{\text{scr}}(\vec{k}) e^{-i\vec{k} \cdot \vec{r}} \quad (8)$$

where $|\vec{k}|$ is the length of the reciprocal vector while N_k is the total k points spread in the first BZ. The result is shown in the inset of FIG. 3(c), where V_x means the real-space screened potential which is also attractive within a certain range of horizontal distance.

C. Superconductivity: Kohn-Luttinger-Like Mechanism

Referring to the Kohn-Luttinger mechanism in Ref. [16], the Cooper pairing interaction mediated by the screened Coulomb potential $V_{\text{scr}}^{\text{ph}}(\vec{q})$ will contribute to superconductivity. In this paper, we only consider the pairings near the Fermi surface with opposite momenta and spins. The analysis of the Cooper pairs finally leads to a self-consistent linearized equation [32] given by:

$$\Delta^{ij}(\vec{k}) = \sum_{i'j'} \sum_{\vec{k}'} \frac{-K_B T}{N_C A_C} V_{\text{scr}}^{\text{ph}}(\vec{k} - \vec{k}') G^{ii'}(\vec{k}', i\hbar\omega) G^{jj'}(-\vec{k}', -i\hbar\omega) \Delta^{i'j'}(\vec{k}') \quad (9)$$

where $G^{ii'}(\vec{k}, i\hbar\omega) = \sum_m \frac{\psi_{m,\vec{k}}^i (\psi_{m,\vec{k}}^{i'})^*}{i\hbar\omega - \xi_{m,\vec{k}}}$ is the Green function [7] with i, i' labelling the atom position in the unit cell lattice while ω stands for the Matsubara frequencies. The Eq. (9) can be rewritten by applying the Matsubara sum [33, 34]:

$$\Delta^{\text{mm}'}(\vec{k}) = \sum_{\vec{k}', \text{nn}'} \Gamma_{\text{mm}'\text{nn}'}(\vec{k}, \vec{k}') \Delta^{\text{nn}'}(\vec{k}') \quad (10)$$

where $\Delta^{\text{mm}'}(\vec{k})$ describes the amplitude of the Cooper pairing between band m and band m' . The Hermitian kernel $\Gamma_{\text{mm}'\text{nn}'}(\vec{k}, \vec{k}')$ can be written as:

$$\begin{aligned} \Gamma_{\text{mm}'\text{nn}'}(\vec{k}, \vec{k}') &= -\frac{1}{N_C A_C} V_{\text{scr}}^{\text{ph}}(\vec{k} - \vec{k}') \\ &\times \langle \tilde{\psi}_{m,\vec{k}} | \tilde{\psi}_{n,\vec{k}'} \rangle \langle \tilde{\psi}_{n',\vec{k}'} | \tilde{\psi}_{m',\vec{k}} \rangle \\ &\times \sqrt{\frac{f(-\xi_{m',\vec{k}}) - f(\xi_{m,\vec{k}})}{\xi_{m',\vec{k}} + \xi_{m,\vec{k}}}} \sqrt{\frac{f(-\xi_{n',\vec{k}'} - f(\xi_{n,\vec{k}}))}{\xi_{n',\vec{k}'} + \xi_{n,\vec{k}}}} \end{aligned} \quad (11)$$

Here, $\Gamma_{\text{mm}'\text{nn}'}(\vec{k}, \vec{k}')$ stands for the element in the kernel matrix, with $\tilde{\psi}_{m,\vec{k}}$ which is the eigenvector of the TB Hamiltonian. In this way, we transform the self-consistent gap equation into the problem of finding the largest eigenvalue of the kernel matrix. Given an appropriate temperature, the eigenvalue of the kernel matrix will be one, which corresponds to the superconductivity under this temperature. Therefore, we diagonalize the kernel matrix to get the largest eigenvalue EV_{max} . $\text{EV}_{\text{max}} = 1$ means that we find the corresponding critical temperature (T_c) of the graphene system.

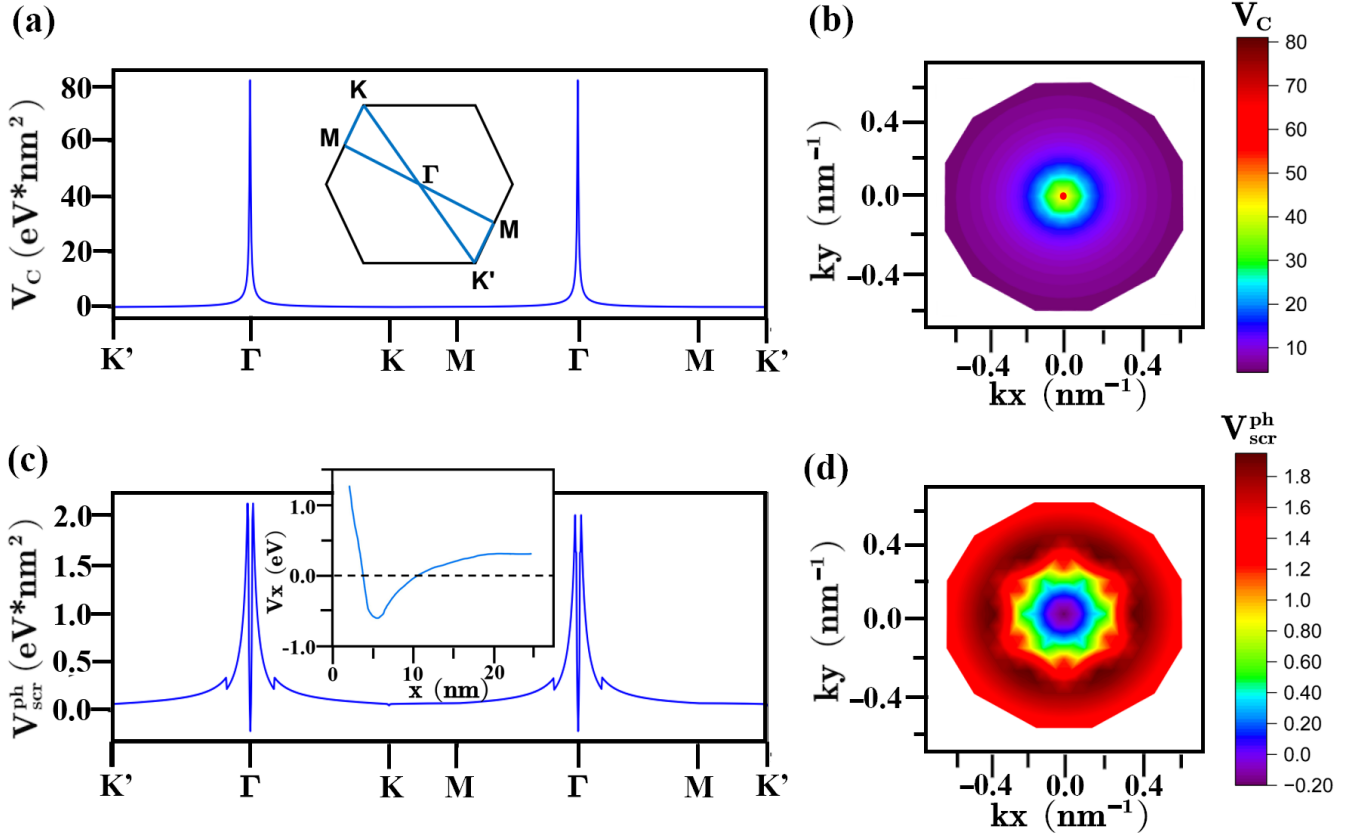


FIG. 3. Screened Coulomb potential in AB graphene with inter-layer potential $\Delta_1 = 100$ meV, temperature $T = 20$ mK and carrier density $n_e = 3.11 \times 10^{11} \text{ cm}^{-2}$. (a) Metallic gate screened potential $V_C(\vec{q})$. The inset shows the high-symmetry path in the first BZ. (b) $V_C(\vec{q})$ near the center Γ in the first BZ. (c) Screened potential $V_{\text{scr}}^{\text{ph}}(\vec{q})$ considering electron-hole excitation and phonon-electron interaction. The inset shows real-space screened potential V_x as a function of the distance x . (d) $V_{\text{scr}}^{\text{ph}}(\vec{q})$ near the center Γ of first BZ with a minimum value $-0.2 \text{ eV} \cdot \text{nm}^2$.

When calculating the T_c we only consider Cooper pairing close to the Fermi surface because only these states will contribute to the superconductivity. We choose the energy cut off $w = 3$ meV which means that only states with $|\xi_{m,\vec{k}}| \leq w$ will be taken into account. That is also the way how we decide \vec{k} and \vec{k}' in the kernel matrix.

III. T_c OF MULTI-LAYER GRAPHENE

A. AB bilayer T_c

Recent experimental detection of superconductivity in AB bi-layer graphene [1] suggests that the critical temperature has a magnitude around 26 mK. Firstly, we apply our mechanism to the T_c calculation in AB bi-layer graphene [35]. The computational results are shown in the FIG. 4(a), where the maximum T_c of graphene systems with different bias $\Delta_1 = 50$ meV, 80 meV, 100 meV are 10 mK, 20 mK and 22 mK. Our calculation results match the experimental value of T_c in the term of magnitude. Compared with recent theoretical work on the superconductivity calculation in bi-layer

graphene[5] with T_c larger than 1K, our results are closer to the experimental detection. These comparison show the prospective reliability of our mechanism.

To further understand the emergence of superconductivity in graphene with applied potential bias, we display the band structures and DOS of AB graphene with three different bias Δ_1 in FIG. 4(b). Interestingly we find that the inter-layer bias applied to graphene will lead to a band gap with the same energy as the bias, which induces the van Hove singularity near the Fermi surface $\mu = \frac{\Delta_1}{2}$. There will be also large DOS peaks close to these Fermi energy, which will contribute to more attractive Coulomb interaction and thus lead to higher critical temperatures. Moreover, we obtain the two-fold degenerate order parameters in AB graphene taking $\Delta_1 = 100$ meV, $T_c = 21.6$ mK and $n_e = 3.11 \times 10^{11} \text{ cm}^{-2}$. The term two-fold indicates that there are two different series of order parameters $\Delta(\vec{k})$ corresponding to the same eigenvalue of the Eq. (10). We plot $\Delta(\vec{k})$ as a function of \vec{k} inside the K and K' valleys respectively, displayed in FIG. 4(c) and (d), where the black lines stand for the Fermi surfaces while the black dot points crossed by these lines represent the van Hove singularities. OP shows the opposite sign of the order parameters in different valleys, which proves the existence of the A_2 symmetry

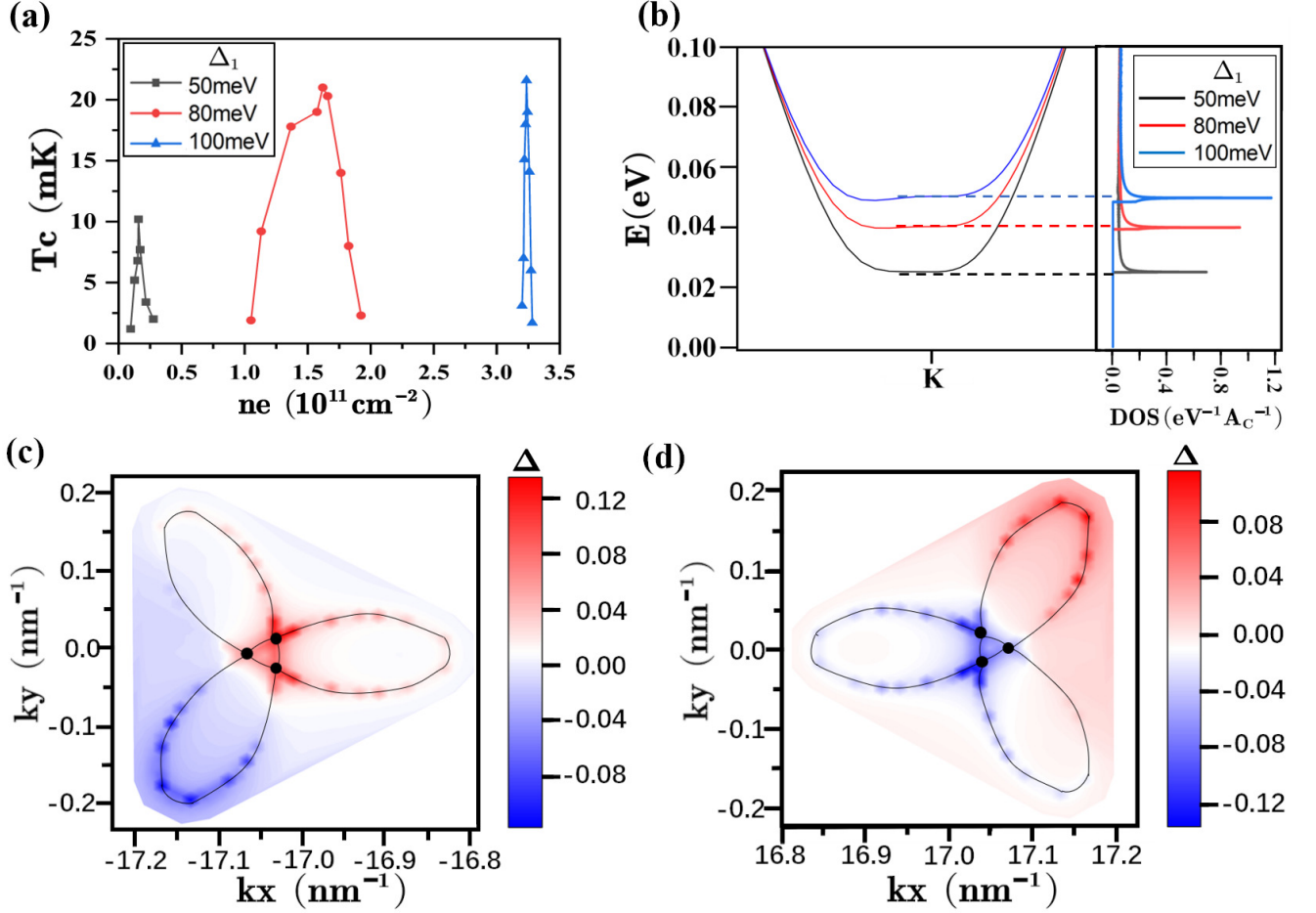


FIG. 4. (a) T_c as a function of the carrier density n_e in AB graphene with different inter-layer potential bias $\Delta_1 = 50, 80, 100$ meV. (b) Bands and DOS close to the charge neutral point. The dashed lines stand for the Fermi energy corresponding to the Dos peaks. (c) Order parameters $\Delta(\vec{k})$ inside the K' valley in AB graphene with $\Delta_1 = 100$ meV, and the black lines represent the Fermi surface. Three black points crossed by these lines represent the van Hove singularities. (d) $\Delta(\vec{k})$ inside the K valley in AB graphene with $\Delta_1 = 100$ meV.

[36, 37]: $\Delta(\vec{k}) = -\Delta(-\vec{k})$ in AB graphene. More importantly, the sign of order parameters will vary inside the valley, which also indicates that the model of the SC dimensionless coupling constant is p wave [11]. As for other multi-layer graphene systems, their $V_{\text{vscr}}^{\text{ph}}$ and OP will display the same behaviour as AB graphene except for difference of magnitude, so we do not show the details of them in this paper. Instead, we focus more on comparing T_c of other multi-layer graphene with different stacking method.

B. Tri-layer graphene T_c

Recent experimental results shows the critical temperature $T_c = 106\text{mK}$ in ABC graphene [2], while the superconductivity in ABA graphene has not been detected. We further apply our mechanism to the superconductivity calculation in two tri-layer graphene systems with ABC and ABA stacking. We selected three inter-layer bias $\Delta_1 = 20$ meV, 50 meV, 80 meV for each tri-layer graphene. As seen in FIG. 5(a), the T_c of

ABC graphene are in good agreement with the experimental observation, with the order of 10^2 mK. Compared with the computation result with T_c up to 3K in Ref. [5], our calculation is more reliable in the term of magnitude. As for another recent work in Ref. [6] displays, its calculated $T_c = 105$ mK in ABC-stacked graphene can help us find suitable parameters including inter-layer bias to obtain a critical temperature closer to the experimental results. Compared with ABC graphene, ABA-stacked graphene has a much lower maximum $T_c = 9.6$ mK as shown in FIG. 5(c). Besides the distinction between critical temperature magnitudes, a sizeable T_c only exists within a certain range of carrier density n_e in ABA-stacked graphene. For example, FIG. 5(a) shows that ABC graphene with $\Delta_1 = 50$ meV has a sizable T_c within the carrier density range up to $5 \times 10^{11} \text{ cm}^{-2}$ while the range of ABA-stacked graphene is only $5 \times 10^{10} \text{ cm}^{-2}$. It means that in experiment the superconductivity could be more observable in ABC-stacked graphene.

The band structures and DOS peaks near van Hove singularities give rise to the different superconductivity critical tem-

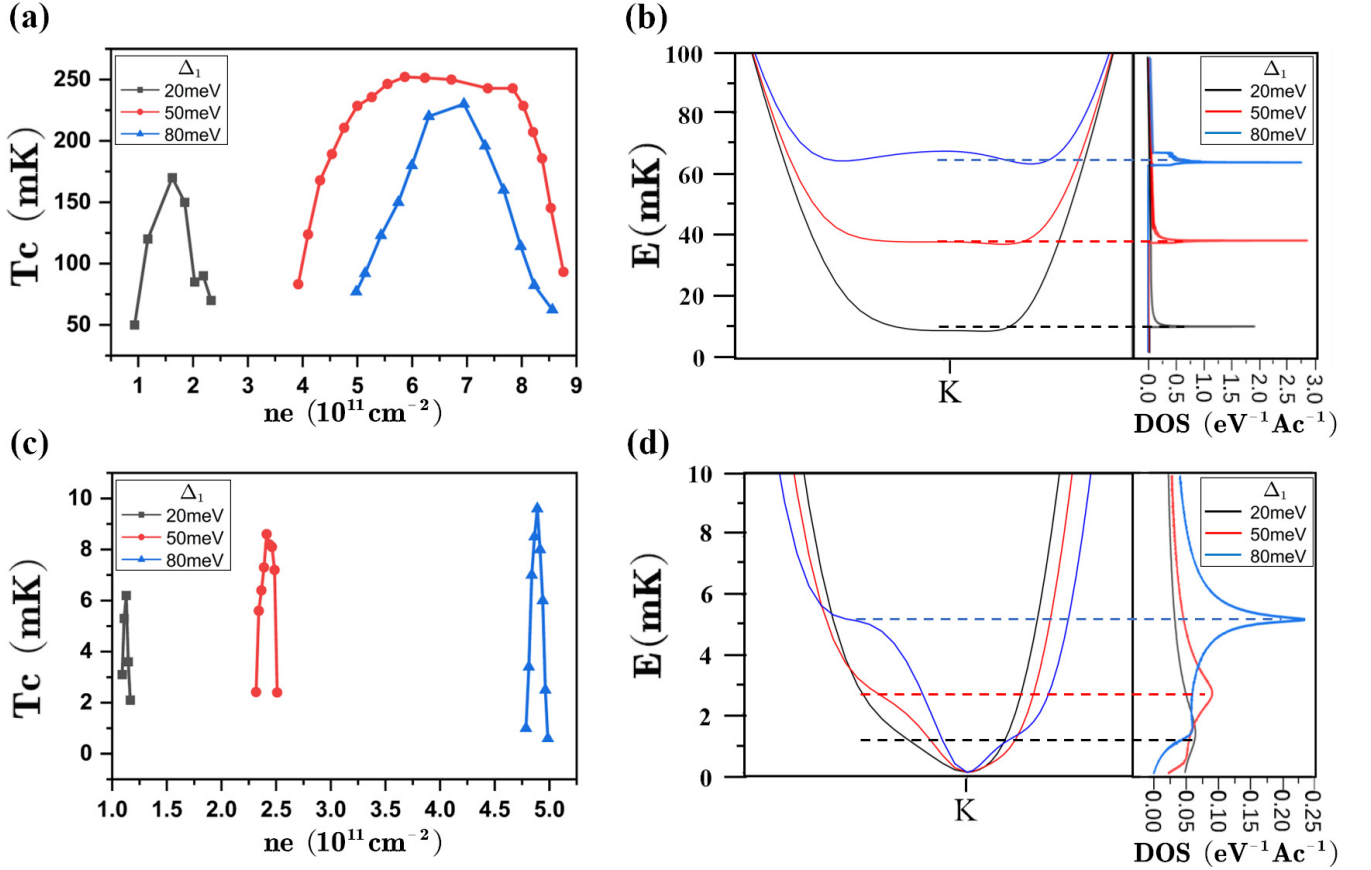


FIG. 5. (a) T_c as a function of the carrier density n_e in ABC graphene with different inter-layer potential $\Delta_1 = 20, 50, 80 \text{ meV}$. (b) Bands and DOS of ABC graphene, which is close to the charge neutral point. The dashed lines stand for the Fermi energy corresponding to the Dos peaks. (c) T_c as a function of the carrier density n_e in ABA graphene. (d) Bands and DOS of ABA graphene.

perature difference in tri-layer graphene systems. In FIG. 5(b) and (d), we find that ABC-stacked graphene has a obvious flat band close to charge neutral point while ABA graphene does not have one. As a result, the DOS maximum of ABC graphene is ten times larger than DOS of ABA graphene, leading to more Cooper pairings near the Fermi surface and higher critical temperatures.

C. Tetra-layer graphene T_c

The superconductivity in tetra-layer graphene has not been detected experimentally. Some theoretial work is done to analyze the critical temperature in ABAC-stacked graphene [5], but there're not existed analysis of superconductivity in the ABAB-stacked graphene system. To completely study the tetra-layer graphene with different stacking methods, we further apply our mechanism to these systems with bias $\Delta_1 = 20 \text{ meV}$, 50 meV , 80 meV . Similar to the regularity found in tri-layer graphene, maximum T_c of ABAC graphene is on the order of 10^2 mK while T_c of ABAB graphene is around 10^1 mK , as displayed in FIG. 6(a) and (c). As for the effective carrier density range, ABAC-stacked graphene with $\Delta_1 =$ has

a range up to $6 \times 10^{11} \text{ cm}^{-2}$, twice larger than the range in ABAB-stacked graphene.

It is obvious to see the influence of DOS on the superconductivity from FIG. 6(b), where the DOS peak of ABAC-stacked graphene with inter-layer bias $\Delta_1 = 50 \text{ meV}$ is much higher than systems with another two bias, 20 meV and 80 meV . From this distinct comparison we learn about the regularity that the graphene system with a higher DOS will usually display a higher T_c , as shown in the FIG. 6(a). As for tetra-layer graphene with ABAB stacking, it has a much more complex DOS distribution near the CNP. In FIG. 6(d) we find that the partial flat band only exists within a small area near the K point. Many DOS peaks appear leading to relative lower DOS near FS compared with graphene with ABAC stacking, ABAB-stacked graphene systems have lower critical temperatures. These results have a meaning of guidance on the experimental detection on tetra-layer graphene superconductivity.

IV. DISCUSSION

We have studied the superconductivity properties in various graphene stackings. High critical temperatures always

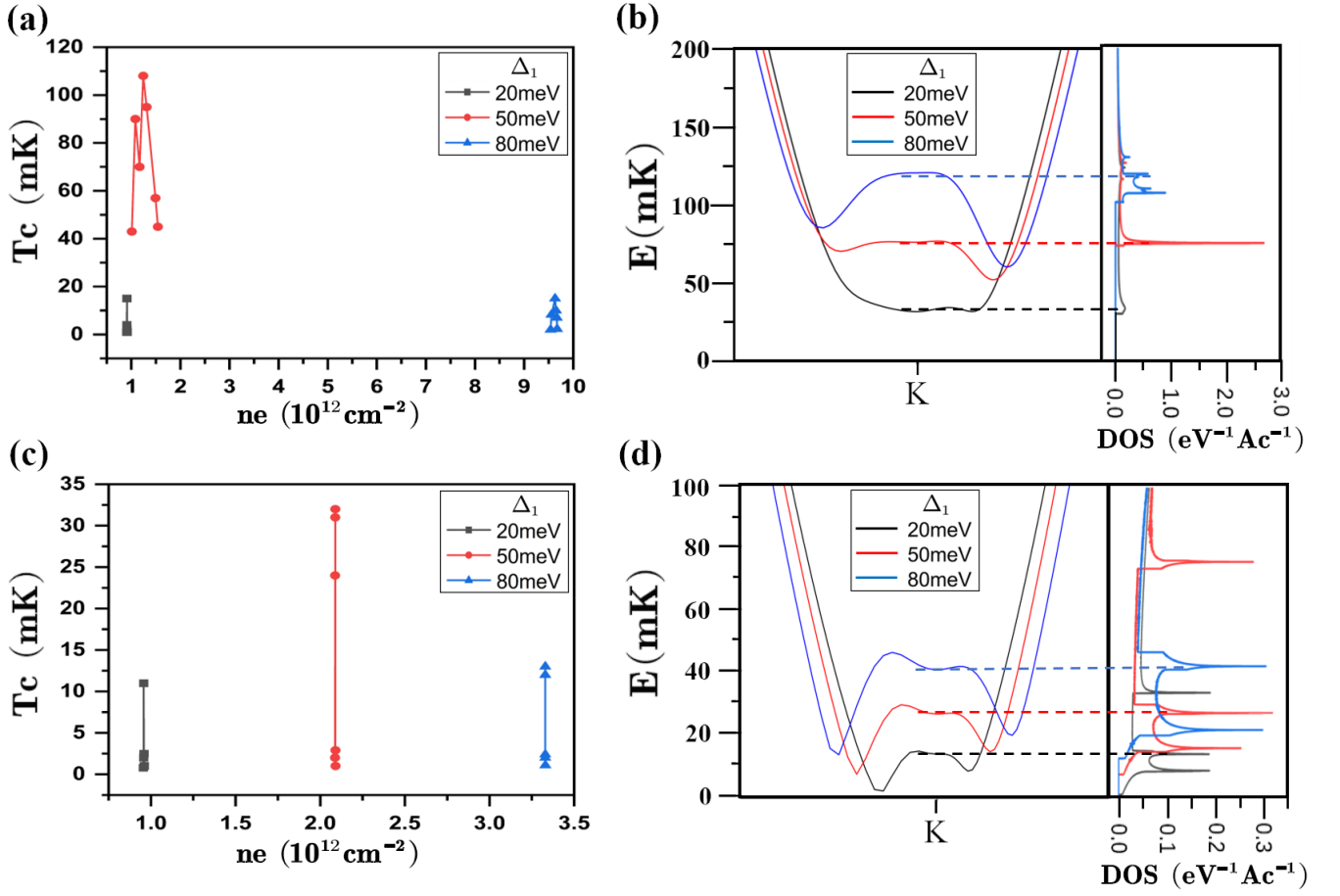


FIG. 6. (a) T_c as a function of the carrier density n_e in ABCA graphene with different inter-layer potential $\Delta_1 = 20, 50, 80 \text{ meV}$. (b) Bands and DOS of ABCA graphene, with dashed lines representing the Fermi energy corresponding to DOS peaks. (c) T_c as a function of the carrier density n_e in ABAB graphene. (d) Bands and DOS of ABAB graphene.

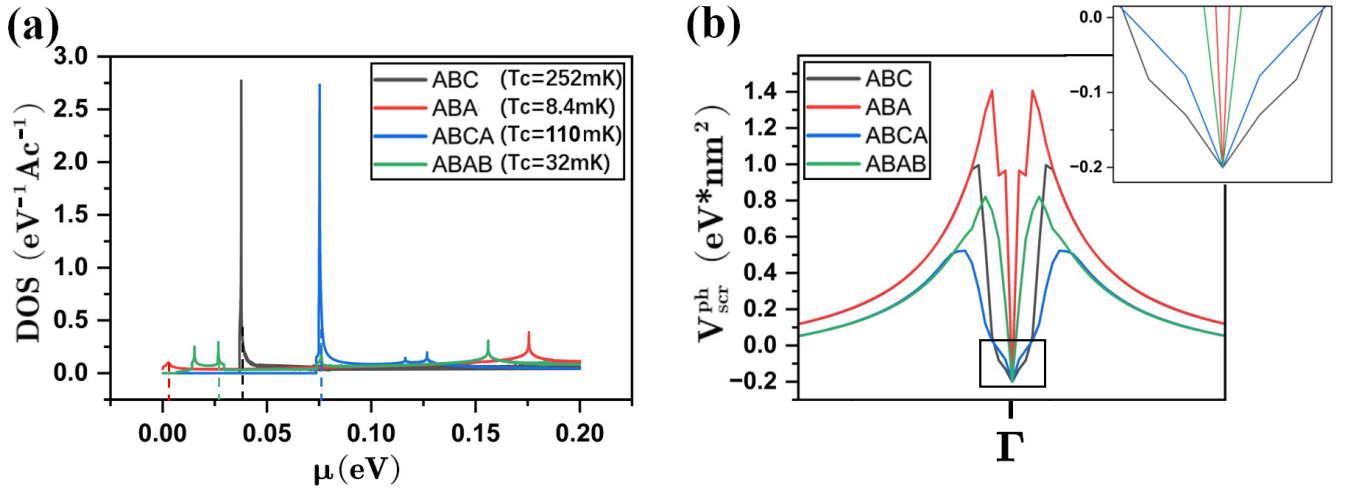


FIG. 7. (a) DOS near the charge neutral point (CNP) in tri-layer and tetra-layer graphene systems with $\Delta_1 = 50 \text{ meV}$. The dashed lines indicate both the van Hove singularities and DOS peaks. (b) Screened potential $V_{\text{scr}}^{\text{ph}}$ in multi-layer graphenes systems with Fermi energy μ corresponding to the DOS peaks and critical temperatures. The inset amplifies the screened potential near Γ inside the black box.

emerge at Fermi surface near large DOS peaks. To show this relation more clearly, we plot the DOS of tri-layer and tetra-layer graphene together in FIG. 7(a). With the same inter-layer bias $\Delta_1 = 50$ meV, the critical temperature is positively correlated with the change of DOS: a larger DOS always corresponds to a higher critical temperature. For example, ABC-stacked and ABCA-stacked graphene systems have much higher DOS peaks than those of ABA-stacked and ABAB-stacked graphene, resulting in more observable superconductivity. It is a meaningful finding because we clarify the strong relation between the superconductivity and stacking method of graphene systems. In particular, our results suggest that ABC(A) stacking will be more beneficial to the appearance of superconductivity. Therefore, it is predicted that multi-layer graphene systems with ABCAB/BABCA stacking, ABCABC stacking, etc. will perform higher critical temperatures than the other graphene with the same number of layers but different stacking method.

A deeper insight to account for this phenomenon is around the screened electron-electron interaction mediated by the acoustic phonons in Feynman diagrams of FIG. 2(a). It is the acoustic phonon-electron interaction which makes the screened potential $V_{\text{scr}}^{\text{ph}}$ attractive near the center of first BZ, and we compare this effect on different graphene systems by putting the screened potential $V_{\text{scr}}^{\text{ph}}(\vec{q})$ in tri-layer and tetra-layer graphene together. The inset in FIG. 7(b) indicates that the minimum screened potentials in different systems will be always the same the constant value in Eq. 4 while $V_{\text{scr}}^{\text{ph}}$ in graphene with ABC stacking and ABCA stacking will converge slower to this constant than others, indicating that the more attractive screened potential effect on a graphene system will lead to its higher critical temperature. We come to a conclusion that a higher DOS peak always represents more attractive screened effect on the Coulomb potential, contributing to a higher T_c [13].

We numerically analyze the critical temperatures in multi-layer graphene based on the Kohn-Luttinger-Like mechanism. The phonon induced charge oscillation contributes to the attractive screened effect on the electron-electron interaction. Our results suggest that this interaction will converge to an attractive constant with momentum near the center of the

first BZ, which is enough for inducing the superconducting states. Other screened effects including metallic gates and electron-hole excitation are also considered in our paper. Our results show that the critical temperatures of AB-stacked, ABA-stacked and ABAB-stacked graphene are in the order of 10^1 mK while those of ABC-stacked, ABCA-stacked graphene are in the order around 10^2 mK. These calculation results about the AB-stacked and ABC-stacked graphene match recent experimental detection [1, 2] very well. Compared with other theoretical work [5–8] on the graphene superconductivity detected in experiments, our work further explores the critical temperature of tetra-layer graphene without existed experimental detection. This exploration can provide the guidance on the future experiments to detect superconductivity in tetra-layer graphene. For example, FIG. 6(a) suggests that ABCA-stacked graphene will perform T_c larger than 100 mK with potential bias $\Delta_1 = 50$ meV and carrier density $n_e = 1.2 \times 10^{12} \text{ cm}^{-2}$. It is worth noting that detectable critical temperatures only exist within a certain range of the carrier density, corresponding to the DOS peaks near the van Hove singularities. Moreover, we obtain the OP in AB graphene, which will change sign within each valley and display intervalley A_2 symmetry. These results about OP indicate that the model of the electron-phonon coupling constant is p wave [38, 39]. Though our computation results match the experimental detection of superconductivity [1, 2] in the terms of magnitude, our analysis has not included all the possible excitation [40, 41] effects, such as the direct electron-phonon interaction and the magnetic ordering. We will further develop our model in the future research.

V. ACKNOWLEDGEMENTS

Note: The numerical calculations in this paper have been done on the supercomputing system in the Supercomputing Center of Wuhan University and TBPlaS software [42] developed by the research group of Prof. Yuan Shengjun at Wuhan University. We wish to acknowledge the support of Tommaso Cea from University of L'Aquila, Pierre Pantaleon, Alejandro Jimeno-Pozo, Héctor Sainz-Cruz from IMDEA Nanoscience Institute and Yunhai Li from Wuhan University.

-
- [1] H. Zhou, L. Holleis, Y. Saito, L. Cohen, W. Huynh, C. L. Patterson, F. Yang, T. Taniguchi, K. Watanabe, and A. F. Young, Isospin magnetism and spin-polarized superconductivity in bernal bilayer graphene, *Science* **375**, 774 (2022).
 - [2] H. Zhou, T. Xie, T. Taniguchi, K. Watanabe, and A. F. Young, Superconductivity in rhombohedral trilayer graphene, *Nature* **598**, 434 (2021).
 - [3] Y. Zhang, R. Polski, A. Thomson, É. Lantagne-Hurtubise, C. Lewandowski, H. Zhou, K. Watanabe, T. Taniguchi, J. Alicea, and S. Nadj-Perge, Spin-orbit enhanced superconductivity in bernal bilayer graphene, *arXiv preprint arXiv:2205.05087* (2022).
 - [4] X. Zhang, K.-T. Tsai, Z. Zhu, W. Ren, Y. Luo, S. Carr, M. Lusk, E. Kaxiras, and K. Wang, Correlated insulating states and transport signature of superconductivity in twisted trilayer graphene superlattices, *Physical review letters* **127**, 166802 (2021).
 - [5] Y.-Z. Chou, F. Wu, J. D. Sau, and S. D. Sarma, Acoustic-phonon-mediated superconductivity in bernal bilayer graphene, *Physical Review B* **105**, L100503 (2022).
 - [6] A. Jimeno-Pozo, H. Sainz-Cruz, T. Cea, P. A. Pantaleón, and F. Guinea, Superconductivity from electronic interactions and spin-orbit enhancement in bilayer and trilayer graphene, *arXiv preprint arXiv:2210.02915* (2022).

- [7] T. Cea, P. A. Pantaleón, V. T. Phong, and F. Guinea, Superconductivity from repulsive interactions in rhombohedral trilayer graphene: A kohn-luttinger-like mechanism, *Physical Review B* **105**, 075432 (2022).
- [8] T. Cea and F. Guinea, Coulomb interaction, phonons, and superconductivity in twisted bilayer graphene, *Proceedings of the National Academy of Sciences* **118**, e2107874118 (2021).
- [9] Y.-Z. Chou, F. Wu, J. D. Sau, and S. D. Sarma, Acoustic-phonon-mediated superconductivity in rhombohedral trilayer graphene, *Physical Review Letters* **127**, 187001 (2021).
- [10] A. Alexandrov and V. Kabanov, Unconventional high-temperature superconductivity from repulsive interactions: Theoretical constraints, *Physical Review Letters* **106**, 136403 (2011).
- [11] A. Ghazaryan, T. Holder, M. Serbyn, and E. Berg, Unconventional superconductivity in systems with annular fermi surfaces: Application to rhombohedral trilayer graphene, *Physical review letters* **127**, 247001 (2021).
- [12] N. Kopnin, T. Heikkilä, and G. Volovik, High-temperature surface superconductivity in topological flat-band systems, *Physical Review B* **83**, 220503 (2011).
- [13] P. K. G. Bedi, Superconducting critical temperature and isotope effect in the presence of electron-phonon, electron-paramagnon and electron-electron interactions in rhodium, *Physica C: Superconductivity and its Applications* **596**, 1354049 (2022).
- [14] T. Cea, N. R. Walet, and F. Guinea, Electronic band structure and pinning of fermi energy to van hove singularities in twisted bilayer graphene: A self-consistent approach, *Physical Review B* **100**, 205113 (2019).
- [15] D. Fil and S. Shevchenko, Electron-hole superconductivity, *Low Temperature Physics* **44**, 867 (2018).
- [16] W. Kohn and J. Luttinger, New mechanism for superconductivity, *Physical Review Letters* **15**, 524 (1965).
- [17] Z. Wu, Y. Han, J. Lin, W. Zhu, M. He, S. Xu, X. Chen, H. Lu, W. Ye, T. Han, *et al.*, Detection of interlayer interaction in few-layer graphene, *Physical Review B* **92**, 075408 (2015).
- [18] E. McCann and M. Koshino, The electronic properties of bilayer graphene, *Reports on Progress in physics* **76**, 056503 (2013).
- [19] J. Lin, W. Fang, W. Zhou, A. R. Lupini, J. C. Idrobo, J. Kong, S. J. Pennycook, and S. T. Pantelides, Ac/ab stacking boundaries in bilayer graphene, *Nano letters* **13**, 3262 (2013).
- [20] M. Aoki and H. Amawashi, Dependence of band structures on stacking and field in layered graphene, *Solid State Communications* **142**, 123 (2007).
- [21] B. Nanda and S. Satpathy, Strain and electric field modulation of the electronic structure of bilayer graphene, *Physical Review B* **80**, 165430 (2009).
- [22] T. Cea and F. Guinea, Band structure and insulating states driven by coulomb interaction in twisted bilayer graphene, *Physical Review B* **102**, 045107 (2020).
- [23] S. Yuan, R. Roldán, and M. I. Katsnelson, Excitation spectrum and high-energy plasmons in single-layer and multilayer graphene, *Physical Review B* **84**, 035439 (2011).
- [24] P. Alonso-González, A. Y. Nikitin, Y. Gao, A. Woessner, M. B. Lundeberg, A. Principi, N. Forcellini, W. Yan, S. Vézé, A. Huber, *et al.*, Acoustic terahertz graphene plasmons revealed by photocurrent nanoscopy, *Nature nanotechnology* **12**, 31 (2017).
- [25] K. Michel and B. Verberck, Theory of the evolution of phonon spectra and elastic constants from graphene to graphite, *Physical Review B* **78**, 085424 (2008).
- [26] P. Verma and R. J. Bartlett, Increasing the applicability of density functional theory. ii. correlation potentials from the random phase approximation and beyond, *The Journal of chemical physics* **136**, 044105 (2012).
- [27] G. P. Chen, V. K. Voora, M. M. Agee, S. G. Balasubramani, and F. Furche, Random-phase approximation methods, *Annual Review of Physical Chemistry* **68**, 421 (2017).
- [28] P. W. Anderson, Random-phase approximation in the theory of superconductivity, *Physical Review* **112**, 1900 (1958).
- [29] E. Hwang and S. D. Sarma, Dielectric function, screening, and plasmons in two-dimensional graphene, *Physical Review B* **75**, 205418 (2007).
- [30] G. Giuliani and G. Vignale, *Quantum theory of the electron liquid* (Cambridge university press, 2005).
- [31] C. Richardson and N. Ashcroft, Effective electron-electron interactions and the theory of superconductivity, *Physical Review B* **55**, 15130 (1997).
- [32] A. Rajagopal and R. Vasudevan, Linearized gap equation for a superconductor in a strong magnetic field, *Physical Review B* **44**, 2807 (1991).
- [33] H. Bruus and K. Flensberg, *Many-body quantum theory in condensed matter physics: an introduction* (OUP Oxford, 2004).
- [34] R. Guérout, A. Lambrecht, K. Milton, and S. Reynaud, Derivation of the lifshitz-matsubara sum formula for the casimir pressure between metallic plane mirrors, *Physical Review E* **90**, 042125 (2014).
- [35] E. F. Talantsev, R. C. Mataira, and W. P. Crump, Classifying superconductivity in moiré graphene superlattices, *Scientific reports* **10**, 1 (2020).
- [36] S. Yip and A. Garg, Superconducting states of reduced symmetry: General order parameters and physical implications, *Physical Review B* **48**, 3304 (1993).
- [37] B. Powell and R. H. McKenzie, Symmetry of the superconducting order parameter in frustrated systems determined by the spatial anisotropy of spin correlations, *Physical review letters* **98**, 027005 (2007).
- [38] P. B. Allen, The electron-phonon coupling constant, *Tc* **500**, 45 (2000).
- [39] T. Koretsune and R. Arita, Efficient method to calculate the electron-phonon coupling constant and superconducting transition temperature, *Computer Physics Communications* **220**, 239 (2017).
- [40] H. He, Y. Sidis, P. Bourges, G. Gu, A. Ivanov, N. Koshizuka, B. Liang, C. Lin, L. Regnault, E. Schoenher, *et al.*, Resonant spin excitation in an overdoped high temperature superconductor, *Physical Review Letters* **86**, 1610 (2001).
- [41] Z. Dong and L. Levitov, Superconductivity in the vicinity of an isospin-polarized state in a cubic dirac band, *arXiv preprint arXiv:2109.01133* (2021).
- [42] Y. Li, Z. Zhan, Y. Li, and S. Yuan, Tbpas: a tight-binding package for large-scale simulation, *arXiv preprint arXiv:2209.00806* (2022).